Caving 2026 – A van As, D Cumming-Potvin & J Wesseloo (eds)

doi:10.36487/ACG_repo/2645_31

# Drawpoint fragmentation analysis and application to flow modelling at Oyu Tolgoi

**Tuul Batbayar** [a,*]

[a] *Rio Tinto, Australia*

## Abstract

*This paper reviews the fragmentation estimates and data collection on Oyu Tolgoi's initial production area. The Hugo North Lift 1 area of the Oyu Tolgoi underground mine is a deep and highly altered orebody, initiating with P0. The size of the P0 cave is approximately 300 × 300 m and 1,300 m below surface. Waste overlies this initial area of roughly 800 m; therefore, fragmentation is critical to understand cave flow. Fragmentation data is collected using an automated photogrammetry tools and manual visual observations. Within this paper, the current analysis is presented which compares actual fragmentation observations with study estimates for P0 and how this data is incorporated in the flow models for the design of future block caving operations.*

**Keywords:** *Oyu Tolgoi, block cave, fragmentation, flow model*

## 1 Introduction

The Panel 0 (P0) block cave within Hugo North Lift 1 (HNL1) orebody is part of the Oyu Tolgoi (OT) porphyry copper–gold mine located in the Umnugovi province of Mongolia. The P0 block cave is highly fractured rock mass located 1,300 m below-surface with significant overlaying waste above. Although the overall rock mass strength is considered fair, mining at this depth still presents challenging geotechnical conditions. As these conditions control the way the rock breaks and moves within the cave, understanding fragmentation becomes essential for interpreting flow behaviour and drawpoint performance at P0.

Figure 1 shows how fragmentation is incorporated into the block caving framework and where it influences key design and performance considerations.

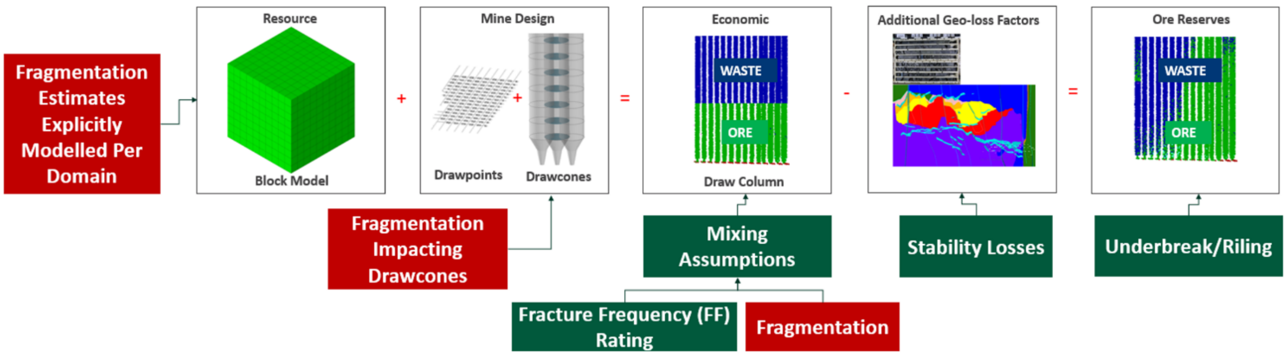


**Figure 1 Explicit method for the integration of geoscience factors in block caving**

* Corresponding author. Email address: tuulb@riotinto.com

In block caving, the fragmentation process is usually grouped into 3 stages: in situ, primary and secondary (Table 1).

**Table 1 Fragmentation classification for block caving (after Brown 2003)**

| Fragmentation | Description |
|---|---|
| In situ | Natural block sizes already present in the rock mass before mining which are controlled by existing joints and structures |
| Primary | Blocks that separate from the cave back when the undercutting is completed and caving initiates |
| Secondary | Additional size reduction as material moves through the draw column under stress, abrasion and interaction |

This classification provides the basis for understanding how fragmentation evolves as the cave develops and moves through the draw column. Figure 2 illustrates how these processes are reflected in the particle size distribution observed at drawpoints.

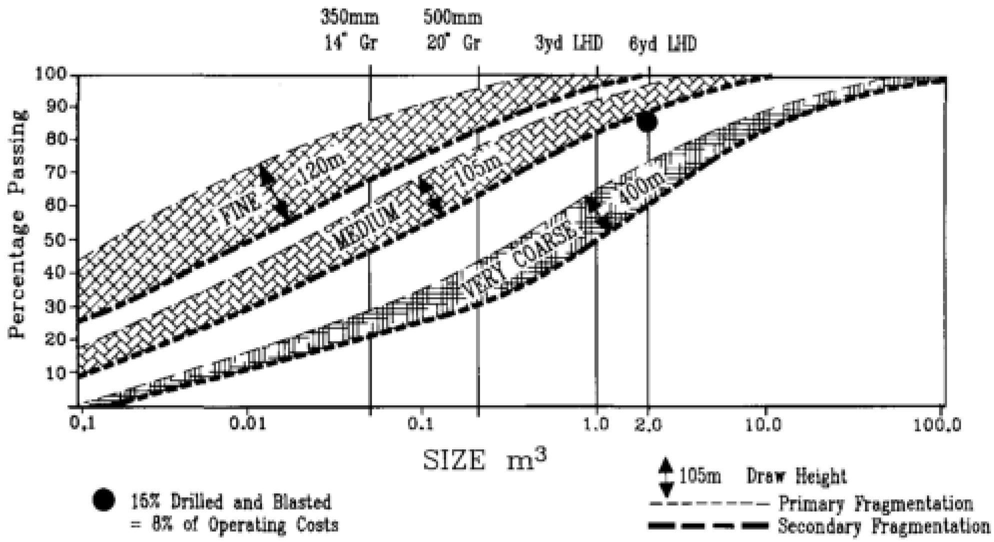


**Figure 2 Size distribution of cave fragmentation (Laubscher 1994)**

The height of draw (HOD), along with other factors such as rock mass strength, stress conditions, and primary fragmentation, influences the fragmentation size distribution, with increasing communition as material travels down the cave column. This shifts the size distribution at the observed drawpoints toward finer material.

# 2 P0 fragmentation estimates based on Block Caving Fragmentation software

The Block Caving Fragmentation (BCF) software is based on a series of analytical methods and empirical rules, predominantly attributed to the work of D Laubscher, which characterise the key processes and factors governing fragmentation behaviour (Guajardo et al. 2022).

## 2.1 Block caving fragmentation domains

BCF fragmentation estimates for HNL1 contain 5 fragmentation domains across the P0 drawpoints. Figure 3 shows the P0 drawpoints represented as coloured circles according to their fragmentation domains with the background showing the clipped fragmentation solids in plan view at the extraction level.

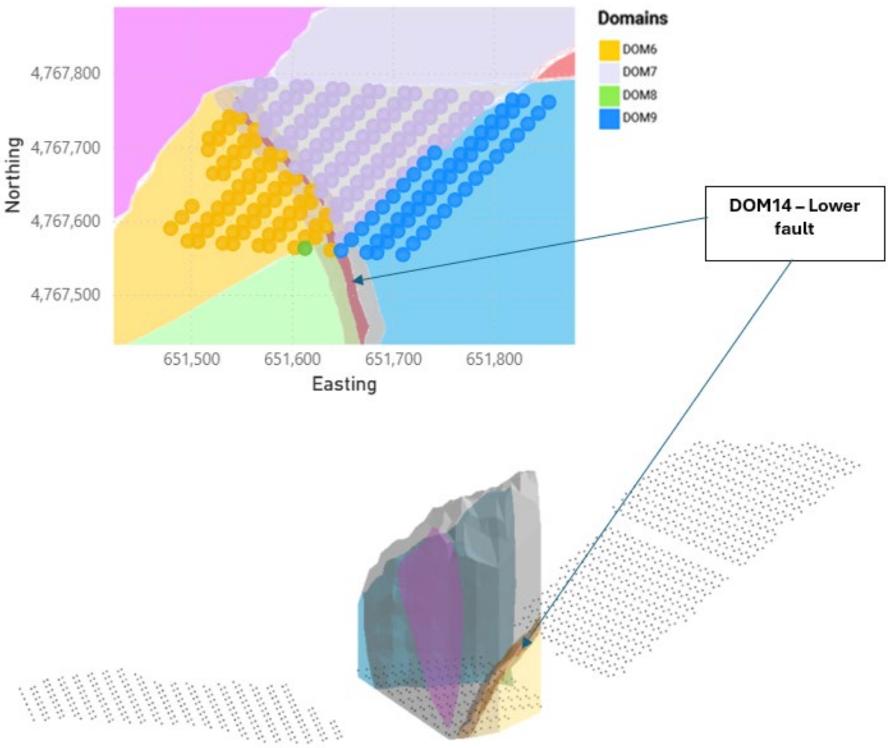


**Figure 3 P0 fragmentation domains at extraction level (EXL): plan and isometric view**

In particular, Domain 14 (Lower Fault) is a bedding parallel anastomosing 6-15 m thick fault zone, consisting of breccia and clay-rich gauge. Due to its thin geometry, observations are limited, making spatial correlation difficult. As a result, the fragmentation domain for Lower Fault drawpoints were assigned to the neighbouring domain value (Figure 3). Therefore, the domains assigned to the drawpoints in Figure 3 are the fragmentation estimates and observations that will be compared to each other.

## 2.2 Fragmentation estimates calibration and application

The BCF curves fall between Laubscher classes 3 and 4, with P0 showing class 3 characteristics in some areas but generally aligning more closely with a class 4 rock mass (Figure 4).

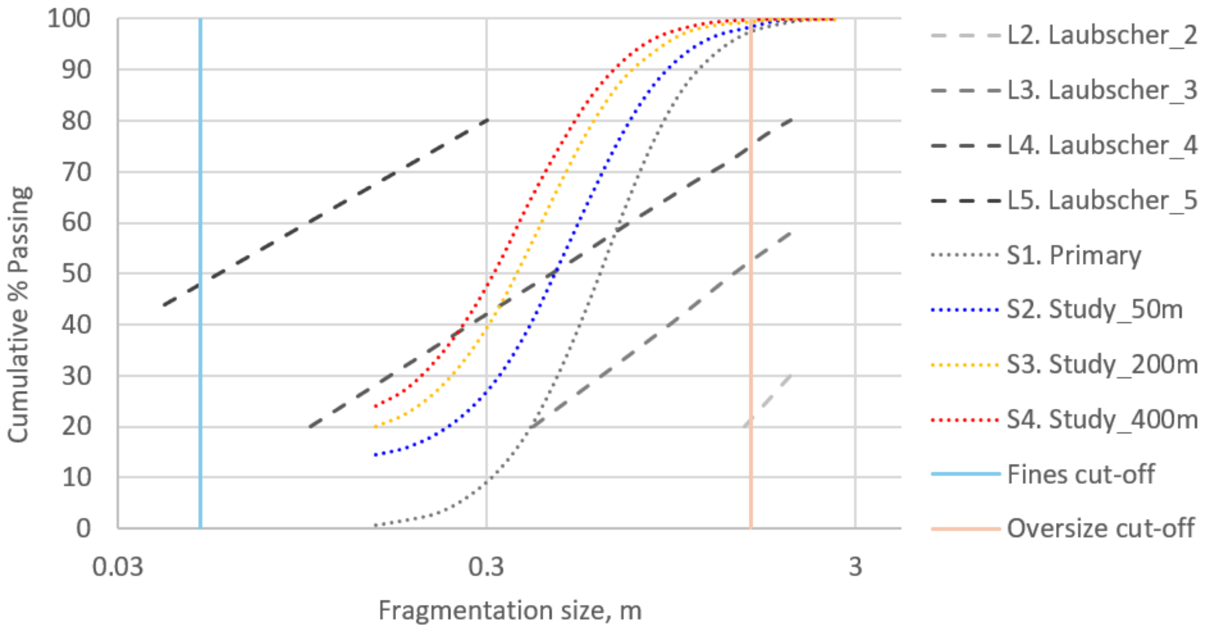


**Figure 4 P0 fragmentation estimates**

The study fragmentation estimate was provided as volumes for block sizes. These values were converted into a length-based dataset to enable direct comparison with fragmentation observations recorded onsite.

To represent irregular rock fragments as simplified spherical models, the equivalent volume diameter was calculated. This allows the mass-based data from sieve analysis to be directly correlated with a diameter:

$$d = \sqrt[3]{\frac{6V}{\pi}} \tag{1}$$

where:

$d$ = the size of the rock fragments was characterised using the volume-equivalent diameter ($d$), defined as the diameter of a sphere with the same volume as the fragment (Wang et al. 2022).

# 3 Site fragmentation observations and data collection

Fragmentation observations are collected from drawpoints in accordance with operational procedure standards. The dataset is structured to support comparison with fragmentation estimates (BCF) and calibration of fragmentation curves.

## 3.1 Data collection and height of draw

The observations were collected through manual visual assessments and an automated photogrammetry tool. Figure 5 shows the introduction of the photogrammetry tool in September 2025 aligns with a noticeable shift in the observed material size distribution, with an increase in fine and small material.

**Figure 5 P0 fragmentation distribution**

This shift may also be influenced by the increasing P0 HOD, averaging around 135 m in April 2026 (Figure 6) with observed values ranging from 76 m in the northeast corner to a maximum of 178 m based on drawn tonnes calculations.

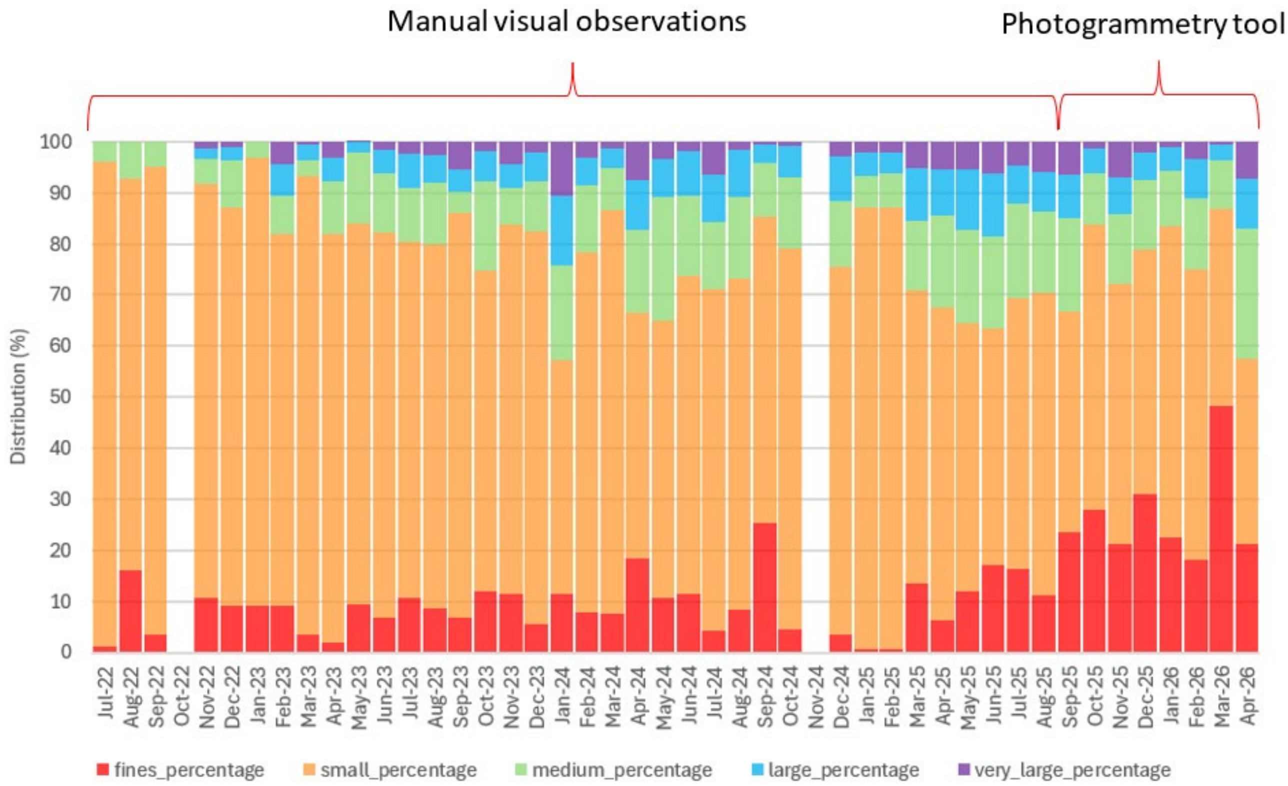


| | 14 | 16 | | 18 | | 20 | | 22 | | 24 | | 26 | | 28 | | 30 | | |
|---|---|---|---|---|---|---|---|---|---|---|---|---|---|---|---|---|---|---|
| | E | W | E | W | E | W | E | W | E | W | E | W | E | W | E | W | E | |
| 17 | 168 | 163 | 177 | 82 | 76 | 111 | 97 | 163 | 132 | 125 | 117 | 120 | 117 | 109 | 105 | 103 | 101 | 17 |
| 16 | 165 | 161 | 176 | 166 | 165 | 115 | 107 | 156 | 132 | 122 | 119 | 121 | 117 | 109 | 104 | 99 | 101 | 16 |
| 15 | 164 | 161 | 166 | 152 | 156 | 114 | 117 | 154 | 128 | 122 | 120 | 124 | 128 | 119 | 112 | 108 | 101 | 15 |
| 14 | 160 | 158 | 156 | 146 | 145 | 104 | 102 | 141 | 129 | 121 | 115 | 121 | 127 | 119 | 114 | 106 | 102 | 14 |
| 13 | 147 | 143 | 152 | 145 | 150 | 115 | 111 | 141 | 127 | 122 | 123 | 130 | 132 | 124 | 112 | 106 | 101 | 13 |
| 12 | 129 | 123 | 146 | 138 | 141 | 127 | 126 | 134 | 127 | 122 | 123 | 129 | 126 | 122 | 116 | 112 | 108 | 12 |
| 11 | | 150 | 149 | 141 | 140 | 129 | 127 | 131 | 124 | 124 | 128 | 134 | 131 | 122 | 115 | 111 | 112 | 11 |
| 10 | | | 153 | 151 | 152 | 135 | 136 | 140 | 135 | 134 | 129 | 136 | 130 | 130 | 123 | 116 | 117 | 10 |
| 09 | | | 161 | 156 | 158 | 137 | 140 | 131 | 125 | 136 | 135 | 137 | 131 | 130 | 128 | 119 | 121 | 09 |
| 08 | | | | | 155 | 137 | 139 | 143 | 138 | 138 | 142 | 134 | 136 | 134 | 133 | 123 | 128 | 08 |
| 07 | | | | | 150 | 138 | 136 | 140 | 150 | 147 | 142 | 141 | 141 | 141 | 138 | 130 | 138 | 07 |
| 06 | | | | 140 | 142 | 135 | 132 | 139 | 146 | 147 | 145 | 145 | 147 | 144 | 144 | 135 | 144 | 06 |
| 05 | | | | 131 | 141 | 134 | 141 | 148 | 154 | 146 | 151 | 148 | 149 | 149 | 147 | 137 | 144 | 05 |
| 04 | | | | 122 | 145 | 136 | 144 | 150 | 158 | 153 | 163 | 160 | 160 | 159 | 158 | 147 | 156 | 04 |
| 03 | | | | | 127 | 114 | 168 | 172 | 177 | 161 | 166 | 164 | 167 | 160 | 162 | 154 | 158 | 03 |

**Figure 6 Height of draw using fragmentation-based drawcones (April 2026 actuals)**

As outlined earlier, secondary fragmentation increases with travel distance in the draw column. With P0 HOD reaching around 135 m, this range best reflects the conditions under which secondary fragmentation is expected to occur and is therefore used for the comparison.

## 3.2 Observation dataset summary

By April 2026, a total of 57,490 fragmentation samples (from 11,498 samples across the 5 datasets) had been collected from the drawpoints (Figure 7), with sample counts per drawpoint ranging from 17–77. To ensure consistent interpretation, the data were grouped into bins based on height of draw, reflecting the transition from blasted (<34 m) to caved material with increasing draw height.

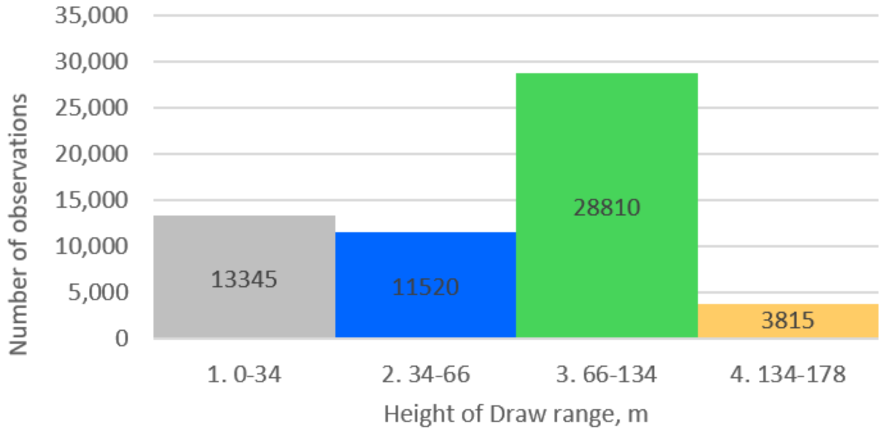


**Figure 7 Distribution of samples by height of draw**

The actual observation data collected within the 66–134 m HOD range is both suitable and representative for comparison against the estimates. This range contains the strongest and most statistically reliable dataset, with a significantly higher number of observations than the other HOD intervals.

## 3.3 Observation fragmentation size classification

Observations are categorised into fixed size classes (fines, small, medium, large, and very large) to standardise variability and enable direct plotting against model assumptions.

Site fragmentation classification (Table 2) spans a range of sizes. Therefore, fixed upper boundary sizes were selected for actuals calculations to enable direct comparison with fragmentation estimates. This approach standardises the data and removes variability within size ranges, ensuring accurate and consistent plotting against the model.

**Table 2 Fragmentation classification (site observation values)**

| Size class | Fragmentation size (mm) | Upper boundary (mm) |
|---|---|---|
| Fines | <50 | 50 |
| Small | 50–500 | 500 |
| Medium | 500–1,000 | 1,000 |
| Large | 1,000–2,000 | 2,000 |
| Very large | >2,000 | 3,368 |

The cumulative percentage passing is referenced to the sieve size, which represents the upper boundary of each particle size interval which reflects the physical aperture through which fragments pass. The upper boundary of the ‘very large’ classification was determined from the BCF limit of 20 $m^3$ and converted to a diameter using Equation 1 (defined in Section 2.1).

# 4 Fragmentation observations versus block caving fragmentation curves

With a representative dataset established for the selected HOD range, the next step is to compare the observed fragmentation with the BCF curves. A direct comparison with the 66–134 m interval (green solid line) cannot be made because the study presents only the 50, 200, and 400 m modelled ranges (dotted lines, Figure 8). However, the 3.66–134 m production actual falls between the 50 and 200 m fragmentation estimates, allowing these modelled ranges to be used as appropriate bounds for comparison.

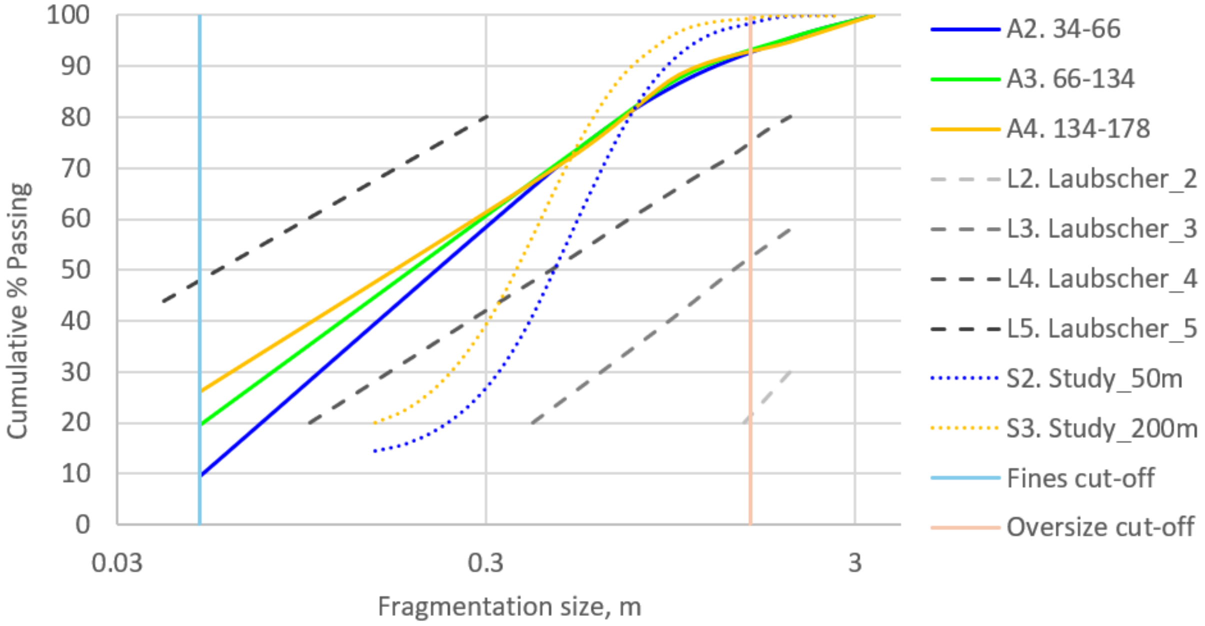


**Figure 8 Actual fragmentation observation by domains versus estimates by height of draw**

Across the analysed dataset, the observed fragmentation is finer than the study estimates, but the P50 values still fall within Laubscher classes 4 and 5 (Table 3).

**Table 3 Laubscher rock mass classification (Laubscher 1994)**

| Rock mass class | 5 | 4 | 3 | 2 |
|---|---|---|---|---|
| Fracture frequency (ff/m) | 50–7 | 20–1.5 | 5–0.4 | 1.5–0.2 |
| Rock size (m) | 0.01–0.3 | 0.1–2 | 0.4–5 | 1.5–9 |

This indicates that the finer observed trend at P0 remains within the expected variability for these rock mass categories which are typically associated with weak, heavily fractured rock masses that break readily under cave conditions.

# 5 Evaluation of observed and predicted fragmentation in kinematic flow

Cellular automata (CA) models adopt a kinematic description of granular flow that is conceptually consistent with Nedderman's kinematic theory, allowing isolated movement zone (IMZ) geometry to emerge from local, particle-scale movement rules. While explicit flow modelling is not undertaken, the analysis is framed within a kinematic framework consistent with the principles underpinning CA-based flow models and Nedderman's theory (Nedderman 1995).

Experimental studies conducted on a range of materials, including rock and across multiple scales, indicate that IMZ width is well described by the kinematic theory of Nedderman (1995). When normalised by mean particle diameter, the theory predicts a consistent relationship between IMZ height and maximum width, as illustrated in Figure 9.

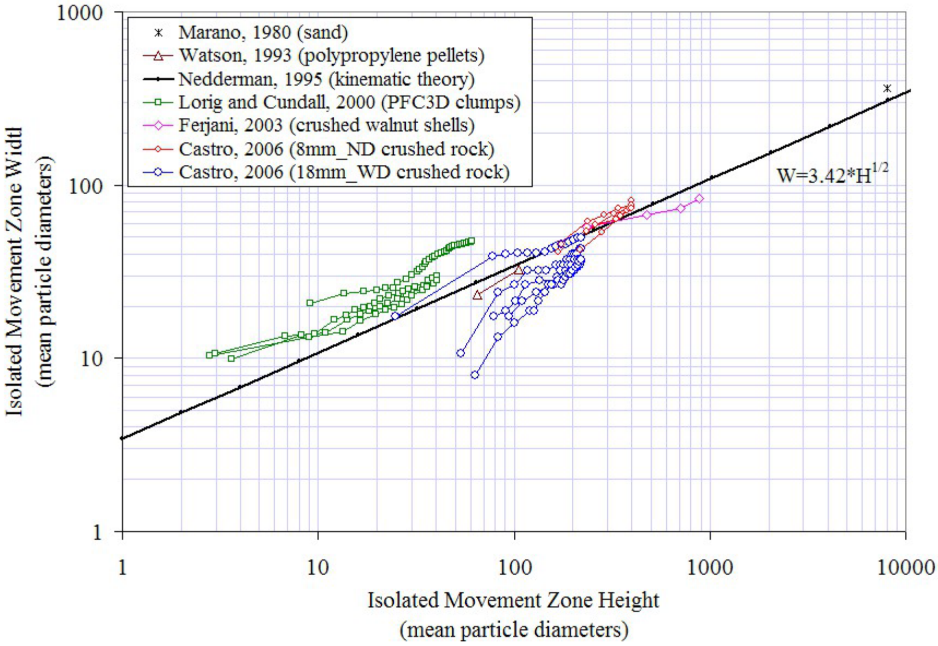


**Figure 9 Isolated movement zone relationship (width versus height) comparison obtained from 3D experiments and simulations is reported by Pierce (2010, Figure 7)**

Accordingly, the Nedderman (1995) kinematic theory curve equation shown in Figure 9 is used to assess the impact of secondary fragmentation which analysed on Section 4. Fragmentation estimates and site actuals were compared using P50 values at 50 m (HOD) for each fragmentation domain. A weighted average P50 value for P0 was then calculated based on the proportional contribution of each domain within the P0 footprint (Table 4).

**Table 4 Flow model fragmentation size (calculated values) – P50 at 50 m height of draw**

| Description | Domain 6 (m) | Domain 7 (m) | Domain 8 (m) | Domain 9 (m) | Weighted average by domain (m) |
|---|---|---|---|---|---|
| Fragmentation estimates | 0.40 | 0.59 | 0.43 | 0.47 | 0.50 |
| Observed diameters | 0.23 | 0.32 | 0.41 | 0.33 | 0.30 |

Table 4 indicates a significant discrepancy between the fragmentation estimates and site actuals. These weighted P50 values are subsequently used to determine IMZ dimensions using the Nedderman equation. The calculated extraction zone geometry is summarised in Table 5.

**Table 5 Extraction zone geometry comparison – based on Nedderman (1995) kinematic theory**

| Description | Fragmentation size (m) | Extraction zone height (m) | Extraction zone width (m) | Radius (m) |
|---|---|---|---|---|
| Fragmentation estimates | 0.50 | 50 | 17.0 | 8.5 |
| Observed diameters | 0.30 | 50 | 13.2 | 6.6 |

These results indicate that variations in secondary fragmentation at 50 m HOD are associated with measurable changes in IMZ radius and corresponding differences in drawcone radius and drawpoint interaction behaviour.

# 6 Conclusion

Overall observations indicate that the P0 rock mass is finer than estimated. This conclusion is based on the complete, up-to-date historical dataset collected throughout the operation. More recent observations indicate a further increase in fines and smaller particle sizes since September 2025 following the introduction of the photogrammetry tool.

While the results remain broadly consistent with the Laubscher classification, the discrepancies between the estimated and observed fragmentation curves exist, particularly in the fines fraction (<50 mm). These differences are likely related to limitations in the estimation approach, as well as challenges associated with capturing fines through both visual observation and photogrammetry. Visual assessments may under-represent finer material due to subjectivity, while photogrammetry can be influenced by resolution constraints and processing assumptions.

Further work is required to better understand the impact of these inter-related occurrences. These findings remain subject to ongoing evaluation as additional data becomes available.

# Acknowledgement

The authors would like to thank Oyu Tolgoi technical and strategic mine planning and geosciences studies team leaders and members for insightful feedback and for supporting us in sharing this work with a broader audience.

# Disclaimer

Please note that this paper contains estimates and forward-looking statements within the meaning of applicable securities laws. These statements are based on publicly available information, operational observations, assumptions, and interpretations available at the time of writing. Actual outcomes may differ due to operational, geotechnical, market, regulatory, and other factors.

# References

Brown, ET 2003, *Block Caving Geomechanics*, JKMRC Monograph Series in Mining and Mineral Processing 3, Julius Kruttschnitt Mineral Research Centre, The University of Queensland, Brisbane.

Guajardo, C, Jakubec, J, Esterhuizen, E, Pichuante, H & Thomas, A 2022, 'The discrete fracture network–block caving fragmentation hybrid method: a new tool to assess fragmentation of block caving mining projects', in Y Potvin (ed.), *Caving 2022: Proceedings of the Fifth International Conference on Block and Sublevel Caving*, Australian Centre for Geomechanics, Perth, pp. 927–938, https://doi.org/10.36487/ACG_repo/2205_63

Laubscher, DH 1994, 'Cave mining: state of the art', *Journal of the South African Institute of Mining and Metallurgy*, vol. 94, no. 10, pp. 279–293.

Nedderman, RM 1995, 'The use of the kinematic model to predict the development of the stagnant zone boundary in the batch discharge of a bunker', *Chemical Engineering Science*, vol. 50, pp. 959–965.

Pierce, M 2010, *A Model for Gravity Flow of Fragmented Rock in Block Caving Mines*, PhD thesis, The University of Queensland, Brisbane.

Wang, L, Jing, H, Yu, J & Liu, X 2022, 'Impact of particle shape, size, and size distribution on gravity flow behaviour of broken ore', *Minerals*, vol. 12, no. 10, article 1183.